Sensors and Actuators B 220 (2015) 107–114

Contents lists available at ScienceDirect

Sensors and Actuators B: Chemical

journal homepage: www.elsevier.com/locate/snb

Highly sensitive biochemical sensor comprising rectangular nanometal arrays

Yue-Jing He*

Department of Electronic Engineering, National Chin-Yi University of Technology, Taichung 41170, Taiwan, ROC

ARTICLE INFO

Article history:
Received 24 March 2015
Received in revised form 20 May 2015
Accepted 21 May 2015
Available online 3 June 2015

Keywords:
Finite element method
Eigenmode expansion method
Perfectly matched layer
Perfectly reflecting boundary condition
Object meshing method
Boundary meshing method

ABSTRACT

This paper proposes a novel design for a highly sensitive high-resolution localized surface plasmon resonance (LSPR) biochemical sensor. The geometrical structure of the sensor consists of three segments. The first segment comprises single-mode fibers located in the output and input ends of the sensor. The second and third segments comprise rectangular nanometal arrays and serve as the analyte regions of the sensor; the amount of displacement between these two segments is one rectangular nonmetal particle. We integrated two breakthrough methods, the object meshing method and the boundary meshing method, with the finite element method to effectively improve the accuracy of simulation outcomes and reduce the amount of time and memory required for performing calculations. Subsequently, we constructed the proposed LSPR biochemical sensor, and the results indicated that the proposed sensor exhibited excellent geometric structure and spectral characteristics. Specifically, the sensor is short (approximately 250 μm) and features high resolution (approximately −130 dB) and high sensitivity (approximately 126,849.1333 nm/RIU).

1. Introduction

In recent years, topics related to surface plasmon resonance (SPR) sensors have attracted substantial attention from scientists, and SPR sensors have been applied in various fields. Generally, SPR sensors can be classified into two categories. The first category comprises propagating surface plasmon resonance (PSPR) sensors with propagation capability. In such sensors, an SPR wave is excited, travels along the metal–analyte interface, and results in both energy propagation and energy loss. An SPR wave forms when the electrons in the metal absorb the energy of an incident light at a specific wavelength; subsequently, the resonant oscillation of the electrons occurs at the metal–analyte interface. The formation of such a wave at the metal–analyte interface enables PSPR sensors to be highly sensitive to changes in the refractive index of an analyte. Therefore, PSPR sensors have been extensively applied in several fields including biology, genetic engineering, and biochemistry [1–15]. The second category comprises localized surface plasmon resonance (LSPR) sensors that have no propagation capability. Such sensors are composed of nanometer-sized metal particles that are insufficiently large for excited LSPR wave propagation. When electrons in the nanometer-sized metal particles of an LSPR sensor absorb the energy of an incident light at a specific wavelength, the resonant oscillation of the electrons occurs at the metal particle–analyte interface and in the space between the metal particles.

Consequently, an LSPR sensor with no propagation capability features more resonance regions than does a PSPR sensor with propagation capability; this characteristic considerably increases the sensitivity of LSPR sensors to changes in target analytes [16–21]. Thus, LSPR sensors have been adopted in numerous fields including chemistry, biochemical sensing, label-free detection, and optoelectronics [22–31].

In our previous studies, we have applied the finite element method (FEM) and eigenmode expansion method (EEM) to design high-efficiency PSPR and LSPR biochemical sensors featuring various architectures [1,16–18]. To improve the accuracy of numerical calculation and reduce the error between simulations and practical operations, we modified the FEM by integrating it with a perfectly matched layer (PML) and perfectly refraction boundary (PRB). However, the FEM developed in our previous studies exhibited major disadvantages. Specifically, in the current numerical simulation methods, uniform triangular meshing is typically the primary technique used. The process of designing PSPR and LSPR biochemical sensors involves installing nanometer-sized metal objects and micrometer-sized waveguide objects in sensor segments. When the uniform triangular meshing method is applied to mesh sensor segments, to ensure that the nanometer-sized

* Tel.: +886 4 23924505; fax: +886 4 23926610.
E-mail address: yuejing@ncut.edu.tw

http://dx.doi.org/10.1016/j.snb.2015.05.068
0925-4005/

metal objects exhibit desirable meshing resolutions, considerable memory space and calculation time are wasted. Therefore, in this paper, we propose two innovative meshing techniques, namely, the object meshing method (OMM) and boundary meshing method (BMM). In the OMM, various resolutions can be used to mesh objects of dissimilar sizes, thereby reducing the amount of unnecessary meshes. In the BMM, high meshing resolutions are applied to the boundary between objects to accurately identify boundary locations and object parameters. The purpose of the present study was to design and analyze a highly sensitive LSPR biochemical sensor by using FEM integrated with OMM and BMM. The results of numerical simulations indicated that the proposed sensor performed excellently and featured the advantages of a short length (approximately 250 μm), high resolution (approximately −130 dB), and high sensitivity (approximately 126,849.1333 nm/RIU).

The remainder of this paper is organized as follows. Section 2 comprehensively introduces the proposed LSPR biochemical sensor, describing the geometrical objects, structural parameters, and material characteristics. In addition, two-dimensional (2D) and three-dimensional (3D) illustrations of the sensor are presented to clarify the arrangements of the rectangular nanometal arrays and the operational principles of the sensor. Finally, the practical aspects of the sensor are discussed and explained.

Section 3 details the techniques (i.e., the PML, PRB, OMM, and BMM) that were integrated with the FEM. According to mathematics, the obtained modes must be pairwise orthogonal. However, according to a numerical simulation method, the orthogonality of modes obtained using the FEM is never 0 because of the limited server memory space and calculation time. In other words, calculation errors are unavoidable when the numerical simulation method is used to perform simulation calculations. Thus, in this study, we used our previously proposed error evaluation standard for determining acceptable calculation errors. Specifically, the meshing resolution applied to the FEM must result in an orthogonality value of less than −40 dB for an obtained mode [16,17]. This section also presents 2D power distribution graphs of the core modes (HE_{11}), discrete LSPR waves, and discrete radiation modes solved using the FEM. According to these graphs, the SPR phenomenon occurred on the surface of and in the space between the metal nanoparticles. This characteristic primarily enables the high sensitivity of the proposed sensor.

Section 4 introduces the EEM, which is based on the Fourier series expansion theory. In the simulation calculation process, the EEM enables the optical wave to propagate energy in the biomedical sensor. According to the Fourier series expansion principle, calculation errors are unavoidable when the amount of expansion bases is insufficient. Therefore, according to our error evaluation standard, the number of modes used in the EEM must be sufficient to ensure that the overall energy loss of the sensor is less than −40 dB [16,17].

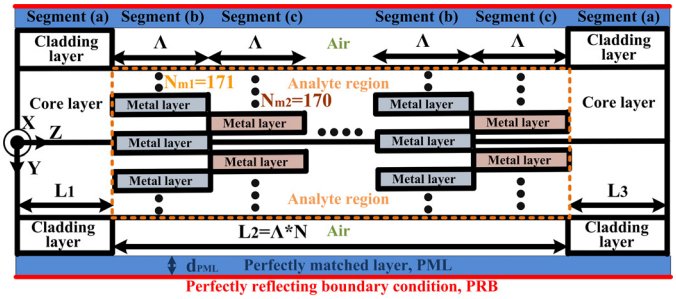

Fig. 2. 2D (*Y*–*Z*) structural illustration of LSPR biochemical fiber sensor.

Section 5 describes designing and analyzing the proposed sensor according to six design and analytical procedures. The results of the simulation are presented as graphs, including the graphs of excited surface plasmon waves, sensitivity analysis, and resolution spectrum analysis. In addition, to investigate the excellent performance of the proposed sensor, its architecture was compared with that of the novel D-shape LSPR fiber sensor [18] and high-performance LSPR biochemical fiber sensor [16].

Section 6 summarizes the proposed sensor and the innovative OMM and BMM. The results confirmed that the proposed sensor performed excellently and had the advantages of a short length (approximately 250 μm), high resolution (approximately −130 dB), and high sensitivity (approximately 126,849.1333 nm/RIU).

2. Novel LSPR biochemical sensor

The novel and highly sensitive LSPR sensor proposed in this study comprises three structurally dissimilar segments. Figs. 1–3 illustrate the 3D, 2D (*Y*–*Z*), and 2D (*X*–*Y*) geometrical structures of these segments, respectively. Segment (a) comprises single-mode fibers and is located on the input and output ends of the biochemical sensor. The procedures involved in constructing Segment (b) are outlined as follows. First, an etching process was applied to the cladding layer of the sensor by engraving a D-shaped cavity without affecting the core layer of the sensor. Next, rectangular nanogold particles were arranged in arrays and plated on the flat surface of the D-shaped cavity. The line extending from the center of the cross-sectional area of the core layer was used as the datum line for arranging the nanometal particles; the nanogold particles were symmetrically arranged on both sides of the datum line, and the duty cycle was 0.5. The procedures used for constructing Segment (c) were similar to those used for Segment (b); the two segments differed only in the arrangements of the nanogold arrays. Specifically, in each column of Segment (b), nanogold particles summing to an odd number were symmetrically arranged on both side of the datum line. In each column of Segment (c), nanogold particles

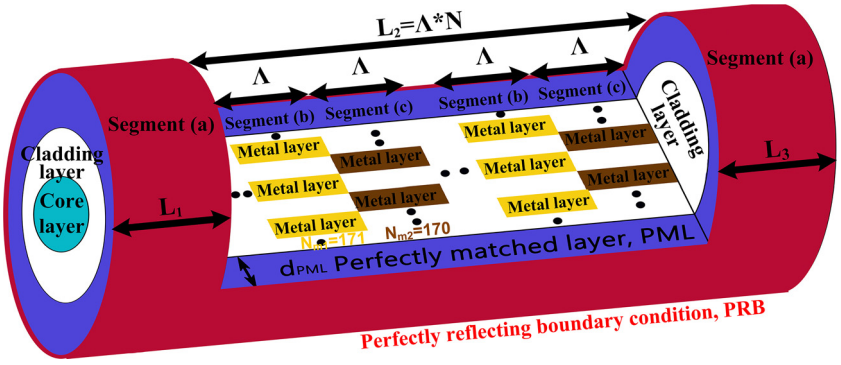

Fig. 1. 3D structural illustration of LSPR biochemical fiber sensor.

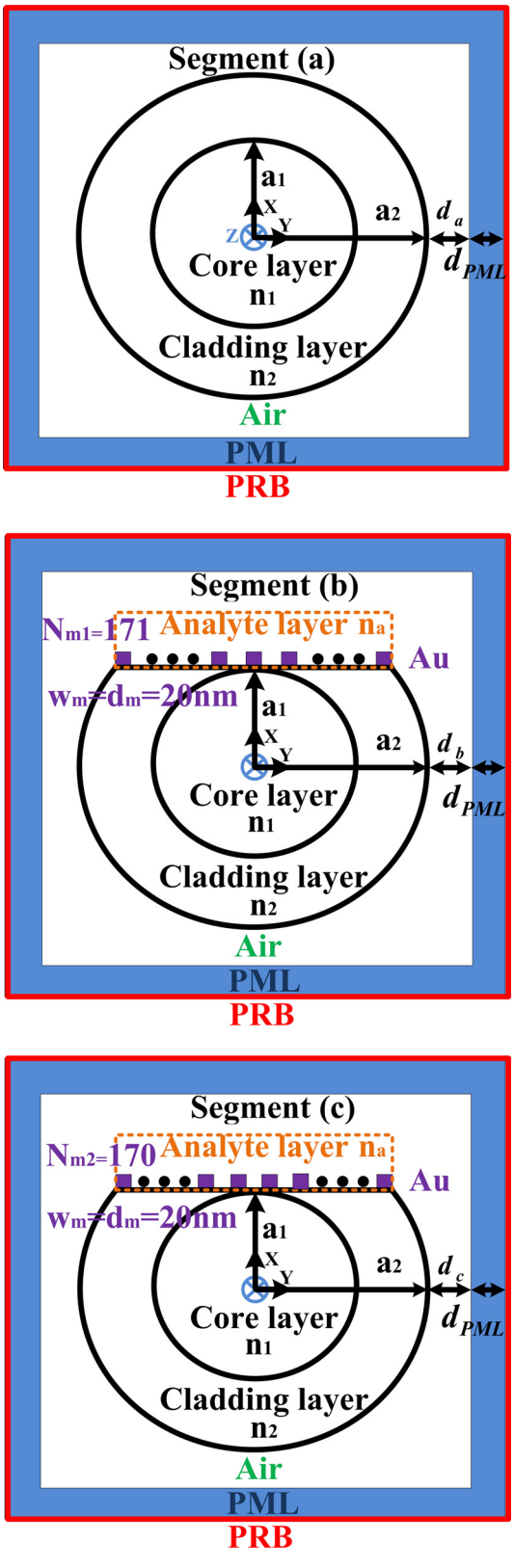

Fig. 3. 2D (X–Y) structural illustration of LSPR biochemical fiber sensor.

summing to an even number were symmetrically arranged on both sides of the datum line. Segment (b) and Segment (c) functioned as the analyte region of the proposed sensor. The operating principle of the proposed sensor can be explained briefly as follows: first, light source enters the sensor from the left side (Fig. 1) and excites the LSPR phenomenon between the nanometal particles. The generation of such a phenomenon indirectly indicates that the nanometal particles cause the input light source to consume energy. Finally, an optical spectrum analyzer is used to measure the output light source emitted from the right side of the sensor. Thus, the spectrum of the sensor is obtained.

The structural and material parameters of the proposed sensor are as follows: $a_1 = 2.25\,\mu m$; $a_2 = 5.25\,\mu m$; $d_m = 0.02\,\mu m$; $w_m = 0.02\,\mu m$; $d_{PML} = 0.825\,\mu m$; $n_1 = 1.454$; $n_2 = 1.43$; $n_a = 1.33$; $d_a = 6\,\mu m$; $d_b = 6\,\mu m$; $d_c = 6\,\mu m$; $n_m = 0.56246309 + j9.840798407$ ($\lambda = 1550\,\mu m$); $N_{m1} = 171$; $N_{m2} = 170$; $\Lambda = 0.1\,\mu m$; $L_1 = 30\,\mu m$; $L_3 = 30\,\mu m$; $N = 1900$; and $L_2 = N \times \Lambda = 190\,\mu m$. The total length of the sensor (L) is 250 μm ($L = L_1 + L_2 + L_3 = 250\,\mu m$). Gold was used to construct the nanometal arrays. According to [1], refractive indices related to wavelengths can be obtained. In the presented parameters, d_{PML} is the thickness of the PML. The numbers of rectangular nanometal particles in each column in Segment (b) (N_{m1}) and Segment (c) (N_{m2}) are 171 and 170, respectively.

Furthermore, n_a is the refractive index of a target analyte covering the surfaces of the nanometal particles. The lengths (Λ) of Segment (b) and Segment (c) are both 0.1 μm, also equal to the length of each rectangular nanometal particle. In the proposed biochemical sensor, the sensing region, consisting of Segments (b) and (c), is arranged in a 0.5 duty cycle. In addition, the total number of nanogold particles in Segments (b) and (c) is 1900. In other words, Segments (b) and (c) each had 950 particles. According to the preceding explanation, the total number of nanogold particles in the sensor was 323,950 ($(171 + 170) \times 950$). Generally, the cross-sectional size of a nanometal particle that triggers an LSPR wave is approximately 20–70 nm. Thus, in the proposed sensor, $d_m = 0.02\,\mu m$, and $w_m = 0.02\,\mu m$; to repeatedly test the sensor that excited SPR waves, the length (Λ) of the rectangular nanometal particles was set as 0.1 μm. Finally, in addition to analyzing the proposed sensor from a theoretical perspective, we investigated its practical operations and applications. The geometric structure of the proposed highly sensitive LSPR biochemical sensor can be actualized using static plowing lithography technology [32].

3. Finite element method

The FEM, a numerical simulation method applied in various engineering fields, is used to solve partial differential equations involving boundary conditions. This method is established according to variational principles, domain meshing, and interpolation functions. We have detailed the FEM in our previous studies [1,16–18]. In the design of and research on LSPR biochemical sensors, the FEM is mainly applied to solve every orthogonal modal base that exists on an X–Y plane.

In any waveguide structure, a complete orthogonal modal base must comprise discrete guided mode and continuous radiation modes. The previously developed FEM and EEM cannot be used to solve continuous radiation modes. However, a highly efficient LSPR biochemical sensor is sensitive to its geometrical structure. Therefore, the existing FEM and EEM must be improved and modified to reduce the error between numerical simulations and practical operations. To create a closed, simulated environment equivalent to an open, realistic environment, we integrated the PML and PRB with the FEM, thereby improving the applicability and accuracy of numerical simulations [16,17].

The FEM developed in our previous studies has severe deficiencies; specifically, the uniform triangular meshing approach is used as the core technique in the numerical simulation. Designing PSPR and LSPR biochemical sensors involves installing nanometer-sized metal objects and micrometer-sized waveguide objects in sensor segments. When the uniform triangular meshing method

is applied to mesh sensor segments, ensuring that the micrometer-sized metal objects exhibit desirable meshing resolutions wastes considerable memory space and calculation time on large-sized objects. Therefore, we propose two innovative methods, the OMM and BMM. In the OMM, various resolutions can be used to mesh objects of dissimilar sizes, thereby reducing the amount of unnecessary meshes. In the BMM, high meshing resolutions are applied to the boundary between objects to accurately identify boundary locations, thereby improving the applicability of object parameters.

Rectangular nanometal particles were essential for improving the sensitivity of the proposed sensor. Consequently, adequately meshing small and large objects became a crucial consideration. We classified the structural components of the sensor into four categories: object boundaries, exquisite objects, moderate objects, and rough objects. According to the proposed meshing methods, triangles were used as the basic elements for meshing the sensor objects, and a meshing ratio of 1:3:30:240 between the rough, moderate, and exquisite objects and the object boundaries was adopted. Fig. 4 indicates that using the BMM resulted in relatively small meshes along the boundary of each object; when the OMM was used, objects were meshed according to their geometrical sizes. The mesh size for metal objects was exquisite, and that for objects in the core layer and cladding layer was moderate. A rough mesh size was applied to objects in the analyte layer.

Figs. 5–7 illustrate the results of various modes solved using the modified FEM. Fig. 5(a) and (b) depicts the core mode (HE_{11}) and discrete radiation mode in Segment (a), respectively. Fig. 6(a) and (b) shows the discrete LSPR wave and discrete radiation mode in Segment (b), respectively. Fig. 6(a) indicates that the SPR phenomenon occurred on the surface of each nanometal particle and in the space between the particles. Fig. 7(a) and (b) illustrates the discrete LSPR wave and discrete radiation mode in Segment (c), respectively. The discrete LSPR waves in Segment (b) and Segment (c) exhibited similar SPR patterns (Fig. 7(a)). According to the physical properties of LSPR, a sensor is highly sensitive to changes in the analyte concentration when the analyte region contains numerous sites that can excite surface plasmons. Consequently, this characteristic enables the proposed sensor to exhibit high sensitivity [16–21]. According to mathematics, the obtained modes must be pairwise orthogonal; that is, the orthogonality of the modes must be 0. However, according to the numerical simulation method, the orthogonality of modes solved using the FEM is never 0 because of limited server memory and calculation time. In other words,

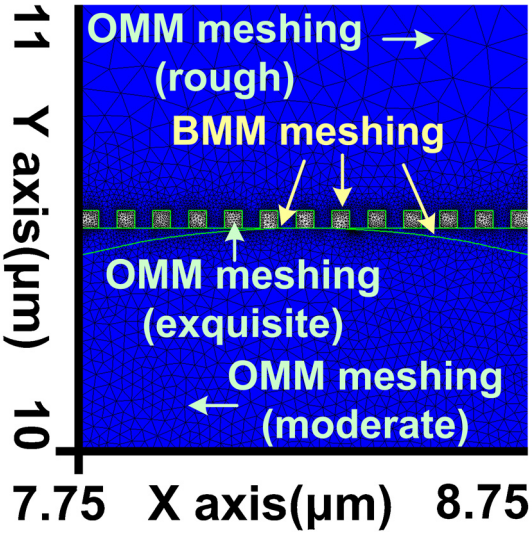

Fig. 4. Sizes of meshes in boundary meshing and object meshing.

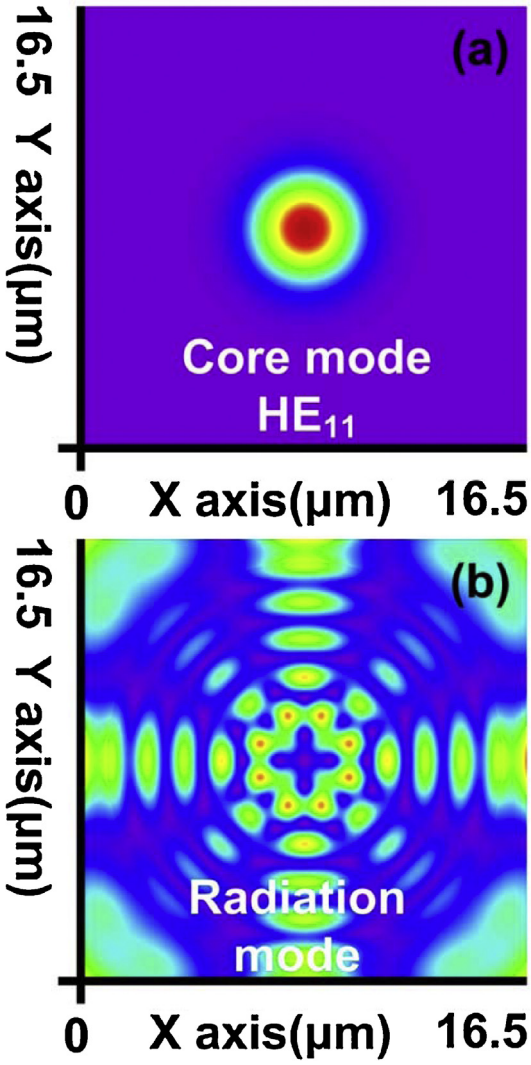

Fig. 5. 2D power distribution graph of Segment (a); (a) core mode (HE_{11}) and (b) radiation mode.

calculation errors are unavoidable when the numerical simulation method is used to perform simulation calculations.

Thus, this study adopted the previously proposed error evaluation standard; that is, the meshing resolution applied to the FEM must result in an orthogonality value of less than −40 dB [16,17]. During the initial stage of sensor design and simulation, a rational meshing resolution was estimated for solving guided modes in the sensor segments. Next, the orthogonality of the obtained guided modes was calculated. When the orthogonality value exceeded −40 dB, the meshing resolution was increased, and the aforementioned process was repeated. The meshing ratio of 1:3:30:240 was applied to mesh objects of dissimilar sizes in the sensor, and the orthogonality of 100 guided modes was calculated (Fig. 8). The results indicated that the meshing ratio resulted in orthogonality values of less than −40 dB. Therefore, the calculation errors were acceptable.

4. Eigenmode expansion method

During the design of the proposed sensor, the EEM was employed to ensure that the guided modes solved using the FEM can propagate energy in sensor segments. The structure of the proposed sensor comprises one SMF segment and two rectangular nanometal array segments with dissimilar pattern arrangements.

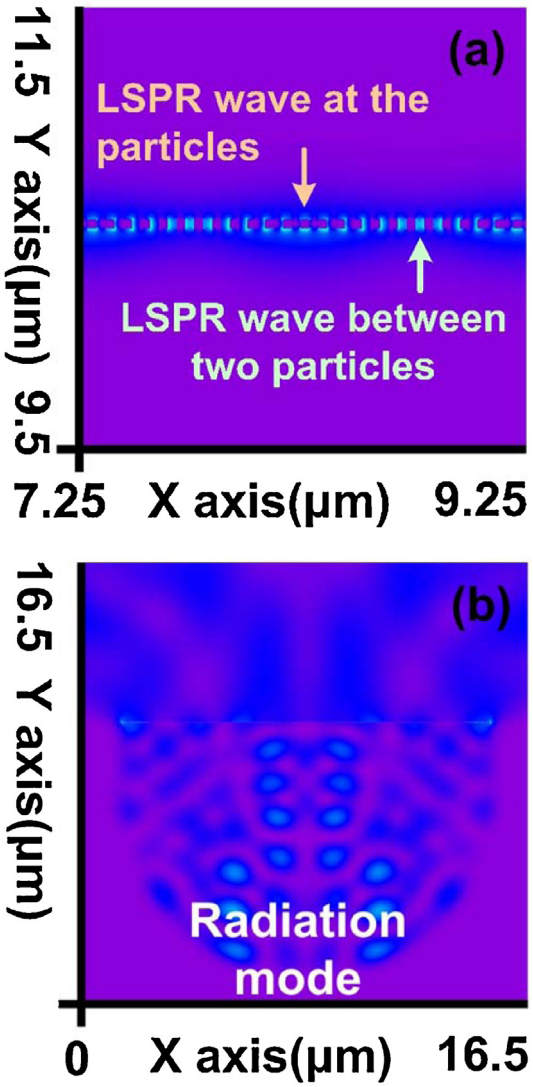

Fig. 6. 2D power distribution graph of Segment (b); (a) LSPR wave and (b) radiation mode.

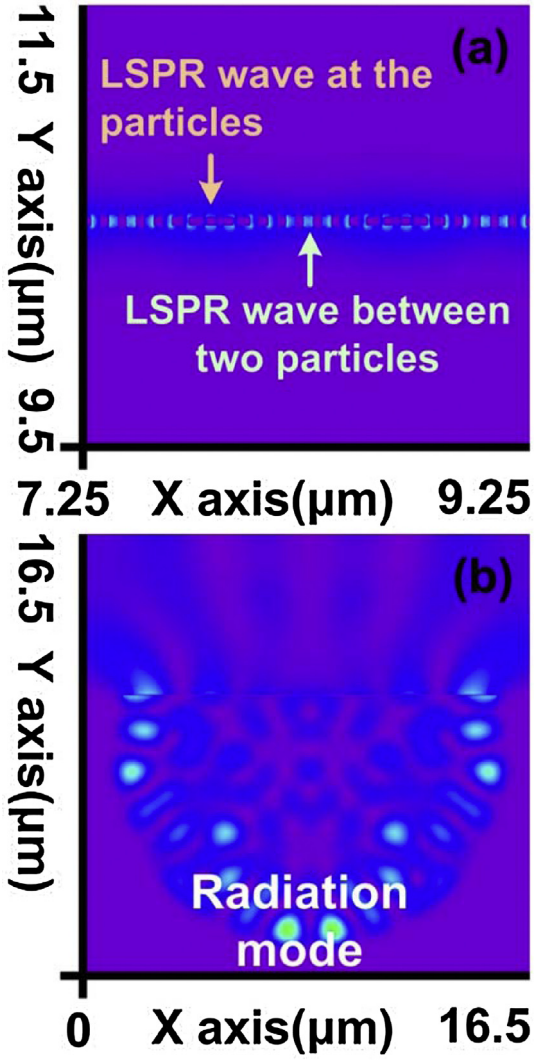

Fig. 7. 2D power distribution graph of Segment (c); (a) LSPR wave and (b) radiation mode.

In the EEM, each column of the segments was considered a uniform guided mode with a fixed refractive index. According to Fig. 9 illustrated in [17], the interface between Segment (K − 1) and Segment (K) is denoted as Junction (J_{k-1}). From a mathematical perspective, the EEM is based on the theory of Fourier series expansion, and Junction (J_{k-1}) is the location at which to execute the Fourier series expansion. According to this theory, calculation errors are inevitable when the number of expansion bases is insufficient. Furthermore, incorporating all modal bases in the sensor structure into the numerical simulation is impossible because of the limited server memory and time required for calculation. Therefore, power loss occurs each time the EEM is executed during the numerical simulation process. Thus, according to the previously proposed error evaluation standard, the number of modes used in the EEM must be sufficient to ensure that the overall sensor energy loss is less than −40 dB [16,17]. During the initial sensor design and simulation, a rational number of modes for executing the EEM was estimated for mode solving. Subsequently, the overall energy loss of the obtained modes was calculated. When the overall energy loss exceeded −40 dB, the number of modes was increased, and the aforementioned procedures were repeated again. For the proposed sensor, a total of 100 modes were used, and the overall energy loss was less than −40 dB (Fig. 9).

5. Design and simulation

According to the geometrical structure of the proposed sensor and to the aforementioned theories, we applied the following six procedures for conducting numerical simulations and performance analysis:

1. The FEM was used to solve 100 guided modes on the *X*–*Y* plane of the sensor.
2. The orthogonality values of the 100 guided modes were verified to determine whether they were less than −40 dB.
3. The EEM was adopted to calculate the energy propagation of the 100 guided modes.
4. Whether the overall power loss during EEM operation was less than −40 dB was verified.
5. The optical spectrum and resolution of the sensor were calculated.
6. The sensor sensitivity to changes in the refractive index of an analyte was determined according to the calculation result of the optical spectrum.

According to the geometrical structural parameters and material parameters mentioned in Section 2, these six procedures were applied to solve the core mode (HE_{11}) of Segment (a), as shown

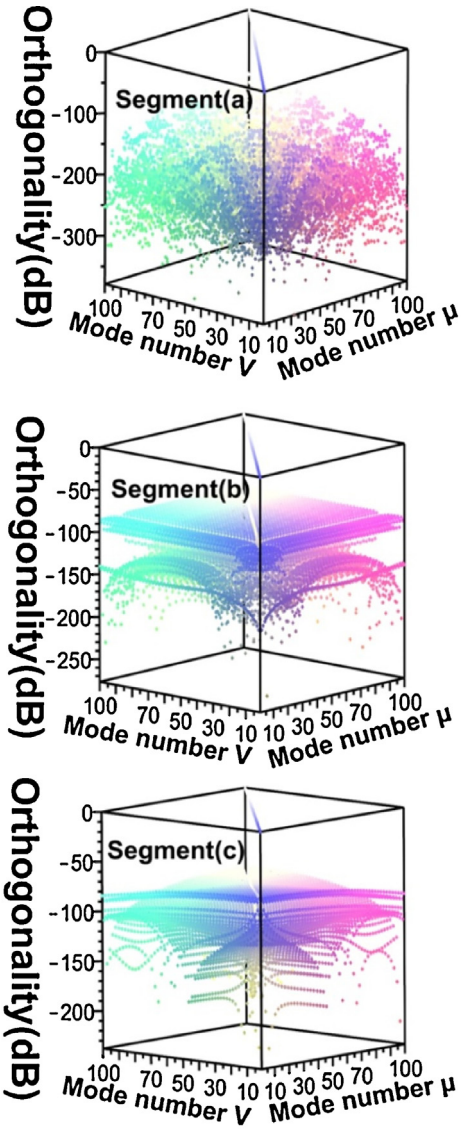

Fig. 8. Orthogonality of 100 guided modes in Segments (a), (b), and (c).

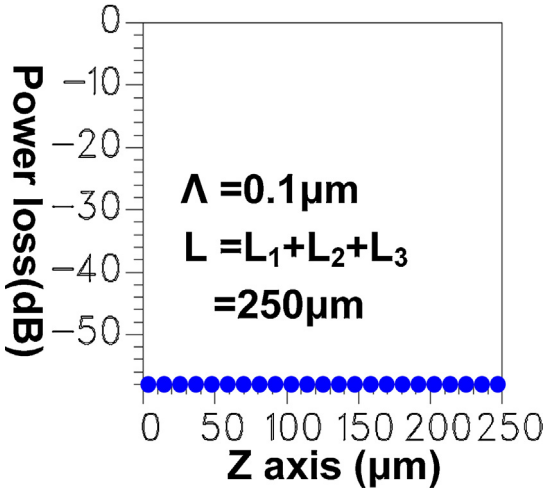

Fig. 9. Relationship between the power loss and length of the proposed sensor when performing EEM.

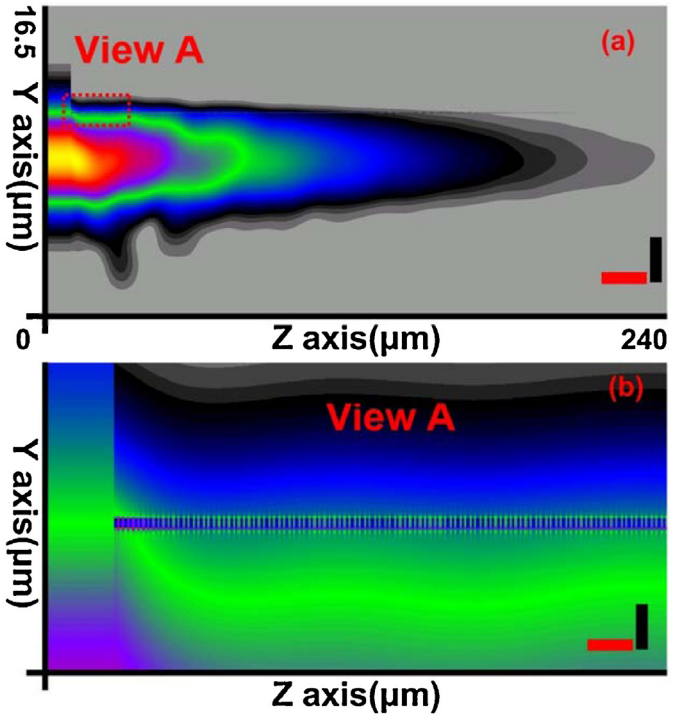

Fig. 10. (a) Power distribution graph of proposed sensor; (b) enlarged display of View A. Scales of the *z*-axis (red) and *y*-axis (black) are 14:115 and 13:115, respectively. (For interpretation of the references to color in this figure legend, the reader is referred to the web version of this article.)

in Fig. 5(a). Furthermore, to verify that the proposed sensor can excite LSPR waves, the core mode was input into the sensor from its left end (Fig. 1), and the energy propagation in the entire sensor was calculated (Fig. 10(a)). To enable clear observation of the LSPR waves, the View A region shown in Fig. 10(a) is magnified in Fig. 10(b), and the ratio scales of the *z*-axis (red) and *y*-axis (black) are 14:115 and 13:115, respectively.

Resolution and sensitivity are essential indicators of sensor performance, which can be easily determined using the spectral characteristics of the sensors [1,16–18]. In the present study, we applied the formula mentioned in previous studies to calculate the optical spectrum of the proposed sensor. Fig. 11 illustrates the change in the optical spectrum of the proposed sensor when the

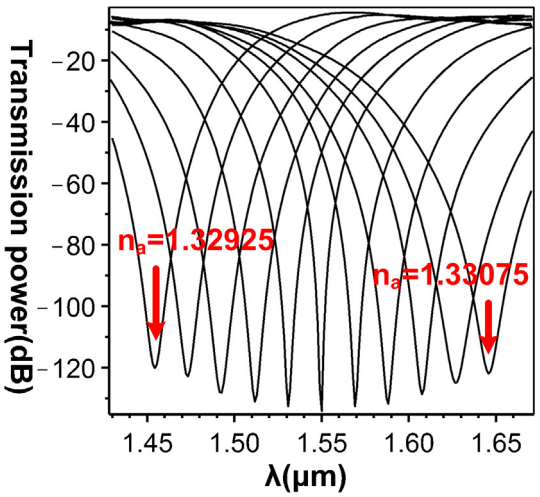

Fig. 11. Change in optical spectrum of the proposed sensor when the analyte refractive index changed from 1.32925 to 1.33075.

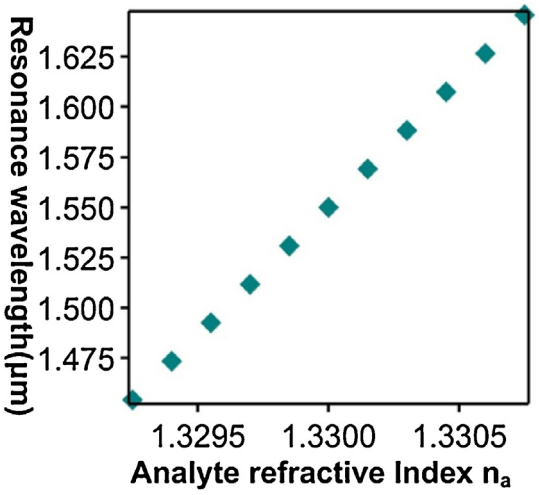

Fig. 12. Change in resonance wavelength of the proposed sensor when the analyte refractive index (n_a) changed from 1.32925 to 1.33075.

analyte refractive index (n_a) changed from 1.32925 to 1.33075. When the design wavelength (λ) was 1550 nm, the resolution of the sensor was −130 dB (Fig. 11). According to Fig. 11, the relationship between the sensor resonance wavelength and the change in the analyte refractive index was determined easily (Fig. 12); when the analyte refractive index (n_a) changed from 1.32925 to 1.33075, the sensor resonance wavelength shifted from 1.4542966 to 1.6445703 μm. According to Fig. 12, the sensitivity of the proposed sensor can be estimated using the following formula:

$$\text{Sensitivity} \approx \frac{1.6445703 - 1.4542966}{1.33075 - 1.32925} \approx 126,849.13333 \left(\frac{\text{nm}}{\text{RIU}}\right)$$

When the electrons in the nanometal particles of LSPR sensors absorb the energy of an incident light at a specific wavelength, the resonance oscillation of the elections occurs at the particle–analyte interface and in the space between the particles. Consequently, an LSPR sensor contains more resonance regions than does a PSPR sensor. This characteristic considerably increases the sensitivity of the LSPR sensor to changes in target analytes. Specifically, an LSPR sensor is highly sensitive when it contains many nanometal particles. The architecture of the proposed sensor was compared with that of two existing sensors. The proposed sensor comprised 323,950 $((171+170)\times 950)$ nanometal particles, and its sensitivity was approximately 126,849.13333 nm/RIU. The novel D-shape LSPR fiber sensor contained 1614 nanometal particles and had a sensitivity of approximately 20,183.33 nm/RIU [18]. The novel and high-performance LSPR biochemical fiber sensor contained 24,000 nanometal particles and had a sensitivity of approximately 93,987 nm/RIU [16]. The simulation results indicated that the proposed sensor performed excellently and featured the advantages of a short length (approximately 250 μm), high resolution (approximately −130 dB), and high sensitivity (approximately 126,849.1333 nm/RIU).

6. Conclusion

The novel and highly sensitive LSPR biochemical sensor proposed in this study comprises three structurally dissimilar segments, namely, one SMF segment and two rectangular nanometal array segments with distinct pattern arrangements. Furthermore, our previously developed FEM, in which the PML and PRB were incorporated, was integrated with the OMM and BMM to improve the meshing techniques. The rectangular nanometal particles in the proposed sensor were key factors for improving sensor sensitivity. In addition, adequately meshing small- and large-sized objects was an essential aspect for developing the proposed sensor. Consequently, the structure of the proposed sensor was divided into object boundaries, exquisite objects, moderate objects, and rough objects. Triangles were used as the basic elements for meshing the sensor objects, and a meshing ratio of 1:3:30:240 among the rough, moderate, and exquisite objects and object boundaries was adopted. The results indicated that the modified FEM effectively facilitated reducing the time and memory required for simulation calculations. According to the geometrical structure of the proposed sensor and relevant theories, six procedures were applied to conduct numerical simulation and performance analysis. The results showed that compared with the other two highly efficient biochemical sensors, the proposed sensor performed excellently and featured advantages such as a short length (approximately 250 μm), high resolution (approximately −130 dB), and high sensitivity (approximately 126,849.1333 nm/RIU).

Acknowledgments

The author gratefully acknowledges the support provided for this study by the Ministry of Science and Technology (MOST 103-2221-E-167-001) of Taiwan.

References

[1] Y.J. He, Investigation of LPG-SPR sensors using the finite element method and eigenmode expansion method, Opt. Express 21 (2013) 13875–13895.
[2] Y. Zhang, H. Li, J. Duan, A. Shi, Y. Liu, Surface plasmon resonance sensor based on spectral interferometry: numerical analysis, Appl. Opt. 52 (2013) 3253–3259.
[3] A. Giorgini, S. Avino, P. Malara, G. Gagliar, M. Casalino, G. Coppola, M. Iodice, P. Adam, K. Chadt, J. Homola, P.D. Natale, Surface plasmon resonance optical cavity enhanced refractive index sensing, Opt. Lett. 38 (2013) 1951–1953.
[4] J. Cao, E.K. Galbraith, T. Sun, K.T.V. Grattan, Cross-comparison of surface plasmon resonance-based optical fiber sensors with different coating structures, IEEE Sens. J. 12 (2012) 2355–2361.
[5] Y. Chen, R.S. Zheng, D.G. Zhang, Y.H. Lu, P. Wang, H. Wing, Z.F. Luo, Q. Kan, Bimetallic chips for a surface plasmon resonance instrument, Appl. Opt. 50 (2011) 387–391.
[6] P. Bhatia, B.D. Gupta, Surface-plasmon-resonance-based fiber-optic refractive index sensor: sensitivity enhancement, Appl. Opt. 50 (2011) 2032–2036.
[7] S. Roh, H. Kim, B. Lee, Infrared surface plasmon resonance in a subwavelength metallic grating under illumination at a large incidence angle, J. Opt. Soc. Am. B 28 (2011) 1661–1667.
[8] M. Gu, P. Bai, E.P. Li, Enhancing the reception of propagating surface plasmons using a nanoantenna, IEEE Photon. Technol. Lett. 22 (2010) 245–247.
[9] M. Nakkach, A. Duval, B. Ea-Kim, J. Moreau, M. Canva, Angulo-spectral surface plasmon resonance imaging of nanofabricated grating surfaces, Opt. Lett. 35 (2010) 2209–2211.
[10] S. Moon, D.J. Kim, K. Kim, D. Kim, H. Lee, K. Lee, S. Haam, Surface-enhanced plasmon resonance detection of nanoparticle-conjugated DNA hybridization, Appl. Opt. 49 (2010) 484–491.
[11] M.J. Sung, Y.F. Ma, Y.F. Chau, D.W. Huang, Surface plasmon resonance in a hexagonal nanostructure formed by seven core shell nanocylinders, Appl. Opt. 49 (2010) 920–926.
[12] S.K. Srivastava, B.D. Gupta, Simulation of a localized surface-plasmon-resonance based fiber optic temperature sensor, J. Opt. Soc. Am. A 27 (2010) 1743–1749.
[13] S.H. Choi, K.M. Byun, Investigation on an application of silver substrates for sensitive surface plasmon resonance imaging detection, J. Opt. Soc. Am. A 27 (2010) 2229–2236.
[14] Y.C. Lu, W.P. Huang, S.S. Jian, Influence of mode loss on the feasibility of grating-assisted optical fiber surface plasmon resonance refractive index sensor, IEEE J. Lightwave Technol. 27 (2009) 4804–4808.
[15] D. Choi, I.M. Lee, J. Jung, J. Park, J.H. Ham, B. Lee, Metallic-grating-based interconnector between surface plasmon polariton waveguides, IEEE J. Lightwave Technol. 27 (2009) 5675–5680.
[16] Y.J. He, Novel and high-performance LSPR biochemical fiber sensor, Sens. Actuators B 206 (2015) 212–219.
[17] Y.J. He, Nanometal ring-array LSPR fiber sensor based on the perfectly matched layer and perfectly reflecting boundary, Sens. Actuators B 202 (2014) 346–356.
[18] Y.J. He, Novel D-shape LSPR fiber sensor based on nano-metal strips, Opt. Express 21 (2013) 23498–23510.
[19] R.A. Awang, S.H. El-Gohary, N.H. Kim, K.M. Byun, Enhancement of field–analyte interaction at metallic nanogap arrays for sensitive localized surface plasmon resonance detection, Appl. Opt. 51 (2012) 7437–7442.

[20] R. Dutta, R. Bharadwaj, S. Mukerji, T. Kundu, Study of localized surface-plasmon-resonance-based optical fiber sensor, Appl. Opt. 50 (2011) E138–E144.
[21] H.Y. Lin, C.H. Huang, C.H. Chang, Y.C. Lan, H.C. Chui, Direct near-field optical imaging of plasmonic resonances in metal nanoparticle pairs, Opt. Express 18 (2010) 165–172.
[22] Y. Lin, Y. Zou, R. Lindquist, A reflection-based localized surface plasmon resonance fiber-optic probe for biochemical sensing, Biomed. Opt. Express 5 (2014) 3935–3948.
[23] C.K. Lee, H.Y. Tseng, C.Y. Lee, S.Y. Wu, T.T. Chi, K.M. Yang, H.Y.E. Chou, M.T. Tsai, J.Y. Wang, Y.W. Kiang, C.P. Chiang, C.C. Yang, Characterizing the localized surface plasmon resonance behaviors of Au nanorings and tracking their diffusion in bio-tissue with optical coherence tomography, Biomed. Opt. Express 1 (2014) 1060–1074.
[24] T. Allsop, R. Neal, M. Chengbo, K. Kalli, D. Webb, Highly sensitive, localized surface plasmon resonance fiber device for environmental sensing, based upon a structured bi-metal array of nano-wires, Opt. Lett. 39 (2014) 5798–5801.
[25] T.T. Chi, Y.C. Tu, M.K. Li, C.K. Chu, Y.W. Chang, C.K. Yu, Y.W. Kaiang, C.C. Yang, Photothermal optical coherence tomography based on the localized surface plasmon resonance of Au nanoring, Opt. Express 22 (2014) 11754–11769.
[26] L. Xie, X. Yan, Y. Du, An aptamer based wall-less LSPR array chip for label-free and high throughput detection of biomolecules, Biosens. Bioelectron. 53 (2014) 58–64.
[27] M.H. Tu, T. Sun, K.T.V. Grattan, LSPR optical fibre sensors based on hollow gold nanostructures, Sens. Actuators B 191 (2014) 37–44.
[28] R.S. Moirangthem, M.T. Yaseen, P.K. Wei, J.Y. Cheng, Y.C. Chang, Enhanced localized plasmonic detections using partially-embedded gold nanoparticles and ellipsometric measurements, Biomed. Opt. Express 3 (2012) 899–910.
[29] P.J. Rivero, A. Urrutia, J. Goicoechea, F.J. Arregui, Optical fiber humidity sensors based on Localized Surface Plasmon Resonance (LSPR) and Lossy-mode resonance (LMR) in overlays loaded with silver nanoparticles, Sens. Actuators B 173 (2012) 244–249.
[30] L. Xu, L.S. Tan, M.H. Hong, Tuning of localized surface plasmon resonance of well-ordered Ag/Au bimetallic nanodot arrays by laser interference lithography and thermal annealing, Appl. Opt. 50 (2011) G74–G79.
[31] K.M. Byun, S.J. Yoon, D. Kim, Effect of surface roughness on the extinction-based localized surface plasmon resonance biosensors, Appl. Opt. 47 (2008) 5886–5892.
[32] L.A. Porter Jr., A.E. Ribbe, J.M. Buriak, Metallic nano structures via static plowing lithography, Nano Lett. 3 (2003) 1043–1047.

Biography

Yue-Jing He received an M.S. degree from the Department of Communication Engineering at National Chiao-Tung University, Hsinchu, Taiwan, in 2000, and a Ph.D. degree from the Department of Electrical Engineering at National Cheng Kung University, Tainan, Taiwan, in 2006. After graduation, in 2008, he joined the faculty of the Electronic Engineering Department, National Chin-Yi University of Technology, Taichung, Taiwan. His research interests are in component design in optical fiber communication and surface plasmon resonance sensors.